PHYSICAL REVIEW C **87**, 011301(R) (2013)

Prolate, oblate, and triaxial shape coexistence, and the lost magicity of $N = 28$ in ^{43}S

M. Kimura,[1] Y. Taniguchi,[2] Y. Kanada-En'yo,[3] H. Horiuchi,[4] and K. Ikeda[5]
[1]*Department of Physics, Hokkaido University, Sapporo 001-0021 Japan*
[2]*Center for Computational Sciences, University of Tsukuba, Tsukuba 305-8571, Japan*
[3]*Yukawa Institute for Theoretical Physics, Kyoto University, Kyoto, Kyoto 606-8502, Japan*
[4]*Research Center for Nuclear Physics, Osaka University, Ibaraki, Osaka 567-0047, Japan*
[5]*RIKEN Nishina Center for Accelerator-Based Science, RIKEN, Wako, Saitama 351-0198, Japan*
(Received 12 August 2012; published 7 January 2013)

We report the low-lying spectrum and collective β and γ deformation of ^{43}S as investigated by antisymmetrized molecular dynamics. Our result successfully explains the observed data including an isomeric $7/2^-_1$ state and illustrates the coexistence of the prolate-deformed ground band with a vanishing $N = 28$ shell gap, a triaxially deformed isomeric state, and an oblate-deformed excited band at very low excitation energies.

DOI: 10.1103/PhysRevC.87.011301 PACS number(s): 21.10.Ky, 21.10.Re, 21.60.−n, 27.40.+z

The erosion of the shell gap and the migration of neutron magic numbers such as $N = 8$ [1] and 20 [2] far from stability have been important and fascinating subjects in nuclear structure physics [3]. The $N = 28$ shell closure in neutron-rich Si and S isotopes has received considerable experimental [4–13] and theoretical attention [14–23]. Experimental data [5,6,8–11] indicate gradual quenching of the $N = 28$ shell gap toward neutron-rich isotones and the onset of deformation in $N \approx 28$ S and Si isotopes. Unlike the case of smaller magic numbers, the neutron single-particle levels $f_{7/2}$ and $p_{3/2}$ that compose the $N = 28$ shell gap belong to the same major shell in the absence of spin-orbit splitting, and their angular momentum differs by 2. Therefore, we can expect that quenching of the $N = 28$ shell gap induces strong quadrupole correlations, which will lead to the coexistence of various deformed states [24]. For example, observation of low-lying states [25] and theoretical calculations [22,23] suggest shape coexistence in ^{44}S.

In the vicinity of ^{44}S, ^{43}S is of particular importance and interest for the following reasons. First, ^{43}S has an odd number of neutrons. Thus, its low-lying spectrum provides direct information on the neutron single-particle levels. Second, and more importantly, it is believed to have a prolate-deformed ground state and a very low-lying isomeric $7/2^-_1$ state at 319 keV, which has been interpreted in the shell model framework as resulting from an inversion of the normal $(\nu f_{7/2})^{-1}$ and deformed intruder $(\nu p_{3/2})^1$ configurations [12]. More recently, measurement of the electric quadrupole moment of the $7/2^-_1$ state [26] has shown that it deviates from the pure spherical $(\nu f_{7/2})^{-1}$ configuration, suggesting possible shape coexistence driven by quenching of the $N = 28$ shell gap and the resulting strong quadrupole correlation. Therefore, a theoretical calculation that can describe the quadrupole collectivity in a large model space is essential for revealing the nature of this shape coexistence far from stability.

In this Rapid Communication, we report triaxial deformation of the isomeric $7/2^-_1$ state and the shape coexistence of prolate, triaxial, and oblate deformation of ^{43}S at excitation energies of less than 2 MeV. We apply the antisymmetrized molecular dynamics (AMD), which has already been successfully applied to the breaking of neutron magic number $N = 8$ [27–29] and 20 [30–32], combined with the generator coordinate method (GCM) using generator coordinates of the quadrupole deformation parameters β and γ. We use the Hamiltonian,

$$H = T - T_g + V_N + V_C, \tag{1}$$

where T and T_g represent the kinetic energies of the nucleons and the center-of-mass motion, respectively. The Gogny D1S interaction [33] is used as the effective nucleon-nucleon interaction V_N, and the Coulomb interaction V_C is approximated by a sum of 12 Gaussians. The variational wave function Φ^π is represented by a parity-projected Slater determinant of deformed Gaussian wave packets [34]:

$$\Phi^\pi = P^\pi \mathcal{A}\{\varphi_1, \varphi_2, \ldots, \varphi_A\}, \quad \varphi_i(\mathbf{r}) = \phi_i(\mathbf{r})\chi_i\xi_i, \tag{2}$$

$$\phi_i(\mathbf{r}) = \exp\left\{-\sum_{\sigma=x,y,z}\nu_\sigma\left(r_\sigma - \frac{Z_{i\sigma}}{\sqrt{\nu_\sigma}}\right)^2\right\},$$
$$\chi_i = a_i\chi_\uparrow + b_i\chi_\downarrow, \quad \xi_i = \{p \text{ or } n\}, \tag{3}$$

where P^π is the parity projector. Because we do not assume any spatial and time-reversal symmetry, there is no difficulty in AMD to describe of the odd-mass system. In this study we discuss the negative-parity states which dominate the low-lying states of ^{43}S. $\mathbf{Z}_i$, a_i, b_i, and ν_σ are the parameters variationally determined with a constraint on the nuclear quadrupole deformation parameters β and γ. The constraint is imposed on discrete sets of (β, γ) on the triangular lattice in the β-γ plane from $\beta = 0$ to 0.75 at intervals of 0.03. A similar constraint on nuclear quadrupole deformation has already been applied in studies of light nuclei by AMD [35,36]. After the variational calculation, we project eigenstates of the total angular momentum from the variational results:

$$\Phi^{J\pi}_{MK}(\beta, \gamma) = P^J_{MK}\Phi^\pi(\beta, \gamma). \tag{4}$$

Here P^J_{MK} is the angular momentum projector. In the following, we refer to the wave function $\Phi^{J\pi}_{MK}(\beta, \gamma)$ as the K state. The calculation is completed by the GCM. The K states $\Phi^{J\pi}_{MK}(\beta, \gamma)$ that have the same parity and angular momentum

but different K values and deformations (β, γ) are superposed:

$$\Phi^{J\pi}_{\alpha} = \sum_{i} \sum_{K=-J}^{J} c_{Ki\alpha} \Phi^{J\pi}_{MK}(\beta_i, \gamma_i), \tag{5}$$

where the quantum numbers except for the total angular momentum and the parity are represented by α, and the rotational motion with respect to any axis is taken into account by the superposition of all possible values of K. The coefficients $c_{Ki\alpha}$ are determined by solving the Hill-Wheeler equation. We call this solution the triaxial GCM. To investigate the effects of triaxial deformation, we also perform a symmetry-restricted GCM calculation, the axial GCM, in which the basis wave functions are limited to the states with $\gamma = 0^\circ$ or 60°. To discuss the fluctuation of the triaxial GCM wave function in the β-γ plane, we use the overlap between the triaxial GCM wave function and the K states:

$$O^{J\pi}_{K\alpha}(\beta, \gamma) = \left| \left\langle \Phi^{J\pi}_{MK}(\beta, \gamma) \middle| \Phi^{J\pi}_{\alpha} \right\rangle \right|^2, \tag{6}$$

which we call the GCM overlap. We comment on the treatment of the pairing correlation. By the variational calculation, we obtain local energy minima with different particle-hole configurations for every given value of β and γ. For example, at the spherical limit, we obtain the local energy minimum with a $(\nu p_{3/2})^{-1}(\nu f_{7/2})^2$ configuration as well as the energy minimum with a $(\nu f_{7/2})^{-1}$ configuration. All of those minima are also included as the GCM basis, and hence, most of the important configurations for the pairing correlation are included in the present calculation, although the coupling with the continuum is missing. As a successful example, readers are directed to Ref. [31] in which the low-lying spectrum of ^{31}Mg is predicted; this spectrum has recently been confirmed by experiments [37].

Before discussing our results, it is helpful to review the present experimental information on ^{43}S. Figures 1(a) and 1(b) show the observed spectra of the $N = 27$ isotones ^{47}Ca and ^{43}S. The 2-MeV shell gap between $0f_{7/2}$ and $1p_{3/2}$ in the spectrum of ^{47}Ca confirms a magicity of $N = 28$. For ^{43}S, five states including the ground state are reported. The isomeric state at 319 keV is identified as $7/2^-$ on the basis of magnetic moment measurement [12], and a $3/2^-$ assignment of the ground state is suggested by the hindered deexcitation from the isomeric state [12]. Thus, the order of the $7/2^-_1$ and $3/2^-_1$ states is inverted. An interesting point is

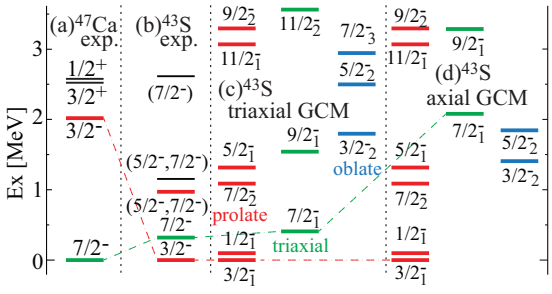

FIG. 1. (Color online) Observed and calculated low-lying spectra of ^{47}Ca and ^{43}S, respectively. Panels (a) and (b) show the observed spectra of ^{47}Ca and ^{43}S. Panels (c) and (d) show the ^{43}S spectra calculated using triaxial and axial GCM, respectively.

that another low-lying $7/2^-$ state is suggested at 940 MeV [8,13]. These two $7/2^-$ states have quite different strengths of the $E2$ transition probabilities to the ground state. The transition from the $7/2^-_1$ state has a strongly hindered value, $B(E2\downarrow) = 0.403\ e^2\ \mathrm{fm}^4$ [12], whereas the 940 keV state has a large value, $B(E2\downarrow) = 87.5\ e^2\ \mathrm{fm}^4$ [7]. These measurements and shell model calculations suggest the shape coexistence of the intruder and normal states [11,12]. In particular, the ground state and the 940-keV state constitute a prolate-deformed ground band with a configuration of $(\nu p_{3/2})^1$, and the isomeric $7/2^-_1$ state is a normal $(\nu f_{7/2})^{-1}$ configuration. Moreover, a recent measurement of the electric quadrupole moment [26] revealed a deviation of the $7/2^-_1$ state from the pure spherical state, which agrees with a shell model calculation using the SDPF-U interaction. The other two excited states at 1.154 and 2.614 MeV are tentatively assigned to the $5/2^-$ or $7/2^-$ states in Ref [13].

Now we examine our results, beginning with Fig. 1(c). The calculated low-lying states can be classified into three groups, the prolate-deformed, triaxially deformed, and oblate-deformed states, as explained below. The ground state is the $3/2^-_1$ state, as suggested in Ref. [12]. It is followed by the $1/2^-_1$ state at 80 keV, the $7/2^-_2$ state at 1.09 MeV, and so forth, which constitute the prolate-deformed $K^\pi = 1/2^-$ rotational band with Coriolis decoupling. The first $7/2^-$ state is located at 410 keV with triaxial deformation. The $9/2^-_1$ state at 1.54 MeV has a triaxially deformed intrinsic structure similar to that of the $7/2^-_1$ state. Finally, the $3/2^-_2$ state at 1.80 MeV is oblate deformed, followed by the $5/2^-_2$ and $7/2^-_3$ states located at 2.49 and 2.94 MeV, respectively. All these low-lying states are deformed; and hence, all values of the $B(E2)$ connecting the states with similar deformations are not small, as listed in Table I. However, the transitions between states with different deformations are hindered; consequently, the $7/2^-_1$ state is long-lived. As shown in Tables I and II, the agreement of the observed excitation energies, $B(E2)$ values, and electromagnetic moments is quite satisfactory without the use of any effective charges or quenching factors. Hence, we can assign the calculated $7/2^-_1$ state to the observed isomeric 319-keV state and the $7/2^-_2$ state to the 940-keV state without ambiguity. Note that the deviation of the $7/2^-_1$ state from a pure spherical state suggested by the $B(E2)$ strength and its quadrupole moment is attributed to triaxial deformation, as explained below.

The characteristics of the three groups can be understood by considering the energy surfaces, the neutron single-particle energies, and the GCM overlap. The negative-parity energy surface before angular momentum projection [Fig. 2(a)] shows that this nucleus is quite soft and flat against both β and γ deformation at $\beta < 0.3$, which is in contrast to the shape-coexisting nuclei with heavier masses such as Zr, Kr, and Pb isotopes where the minima with different deformations are well separated by the potential barrier [38]. In this region, the $N = 28$ shell gap varies and even vanishes depending on β and γ, which is confirmed by the neutron single-particle energies in Fig. 3 calculated using the AMD + Hartree-Fock method [39]. The $N = 28$ shell gap which is approximately 4 MeV at a spherical shape decreases rapidly as the prolate deformation grows and the intruder orbit originating in the

TABLE I. Calculated $B(E2; J_i \to J_f)$ and $B(M1; J_i \to J_f)$ strengths. Numbers in parentheses are the observed values [7,12]. $B(E2)$ values smaller than 5 $e^2\,\mathrm{fm}^4$ are not shown, except for the transition from the $7/2_1^-$ state to the $3/2_1^-$ state. In the first column, p, t, and o denote prolate-deformed, triaxially deformed, and oblate-deformed states, respectively.

Def.	J_i	J_f	$B(M1)$ (μ_N^2)	$B(E2)$ $(e^2\,\mathrm{fm}^4)$
p → p	$3/2_1^-$	$1/2_1^-$	0.17	90.1
	$5/2_1^-$	$1/2_1^-$	–	91.7
	$5/2_1^-$	$3/2_1^-$	0.05	24.6
	$7/2_2^-$	$3/2_1^-$	–	100.6 (87.5)
	$7/2_2^-$	$5/2_1^-$	0.18	14.3
	$9/2_2^-$	$5/2_1^-$	–	132.4
	$9/2_2^-$	$7/2_2^-$	0.05	7.8
	$11/2_1^-$	$7/2_2^-$	–	108.9
	$11/2_1^-$	$9/2_2^-$	0.08	15.4
t → t	$9/2_1^-$	$7/2_1^-$	0.48	115.9
	$11/2_2^-$	$7/2_1^-$	–	22.1
	$11/2_2^-$	$9/2_1^-$	0.53	87.6
o → o	$5/2_2^-$	$3/2_2^-$	0.34	109.8
	$7/2_3^-$	$3/2_2^-$	–	39.9
	$7/2_3^-$	$5/2_2^-$	0.54	68.2
t → p	$7/2_1^-$	$3/2_1^-$	–	0.1 (0.45)
t → o	$7/2_1^-$	$3/2_2^-$	–	13.4
	$7/2_1^-$	$5/2_2^-$	0.02	8.9
	$9/2_1^-$	$5/2_2^-$	–	13.3

spherical $p_{3/2}$ level appears around $\beta = 0.2$. At large prolate deformation ($\beta > 0.3$), the $N = 28$ shell gap is completely lost. In the triaxially deformed region, the order of the orbits originating in the spherical $f_{7/2}$ and $p_{3/2}$ levels is reversed, and for $\beta = 0.3$, the reversal occurs around $\gamma = 20°$. On the oblate side, the intruder orbit stays much higher than $f_{7/2}$ and the $N = 28$ magicity is maintained well. Therefore, at large prolate deformation the intruding $(\nu p_{3/2})^1$ configuration dominates, whereas the normal $(\nu f_{7/2})^{-1}$ configuration dominates the oblate side, and both normal and intruder configurations coexist in the triaxial region. This behavior of the neutron single-particle levels qualitatively agrees with that of ^{44}S [17].

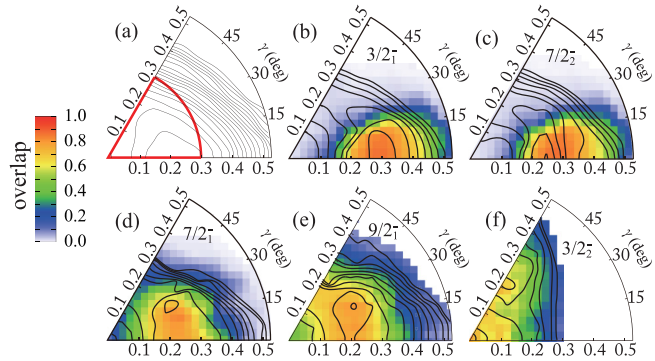

FIG. 2. (Color online) (a) Negative-parity energy surface in the β-γ plane obtained by variation after parity projection. The red line shows the deformation path along which the neutron single-particle energies are shown in Fig. 3. (b)–(f) Energy surfaces and GCM overlaps. Contours show the energy surface at intervals of 1 MeV for the K state which has the largest overlap with each state. Color plots show the GCM overlap with the K state.

We examine the nature of the low-lying states by referring to the GCM overlap (Fig. 2) and the behavior of the $N = 28$ shell gap (Fig. 3). The ground state is dominated by the $K^\pi = \pm 1/2^-$ states; the contour in Fig. 2(b) shows its energy surface. The GCM overlap between the ground state and the $K^\pi = 1/2^-$ state, shown by the color plot in Fig. 2(b), is concentrated in the prolate-deformed region with $\beta > 0.2$ and $\gamma < 20°$, which means that the intruder $(\nu p_{3/2})^1$ configuration is dominant. The $7/2_2^-$ state [Fig. 2(c)] has a quite similar nature; i.e., $K^\pi = \pm 1/2$ states are the dominant component of this state and the GCM overlap is concentrated in the prolate side. This shows that the ground state and the $7/2_2^-$ state belong to the same rotational band and explains the origin of the large $B(E2)$ between them. Other states with prolate deformation, such as the $1/2_1^-$ and $5/2_1^-$ states also dominated by the $K^\pi = \pm 1/2^-$ states, their GCM overlap have maxima in the prolate-deformed region as listed in Table II. The electromagnetic properties of these band members (Tables I and II) also support the "particle plus rotor" nature. To experimentally confirm the

TABLE II. Calculated excitation energies, deformation parameters, and electromagnetic moments. Numbers in parentheses are the observed values [12,13,26]. The deformation parameters are the averaged value weighted by the squared GCM amplitude $|c_{Kia}|^2$ in Eq. (5).

Def.	J^π	E_x (MeV)	β	γ (deg.)	Q ($e\,\mathrm{fm}^2$)	μ (μ_N)
p	$3/2_1^-$	0.0	0.32	6	−13.2	−0.60
	$1/2_1^-$	0.08	0.30	6	–	0.71
	$7/2_2^-$	1.09	0.30	8	−22.0	−0.24
	$5/2_1^-$	1.32	0.29	7	−20.1	1.45
	$11/2_1^-$	3.07	0.26	8	−25.4	0.41
	$9/2_2^-$	3.29	0.30	8	−21.4	1.26
t	$7/2_1^-$	0.41(0.319)	0.24	23	26.1 (23)	−1.08(−1.11)
	$9/2_1^-$	1.54	0.28	27	7.28	−0.19
	$11/2_1^-$	3.52	0.21	21	−5.35	0.41
o	$3/2_2^-$	1.80	0.13	56	12.1	−0.82
	$5/2_2^-$	2.49	0.16	53	−7.0	0.14
	$7/2_3^-$	2.94	0.15	51	−11.1	0.39

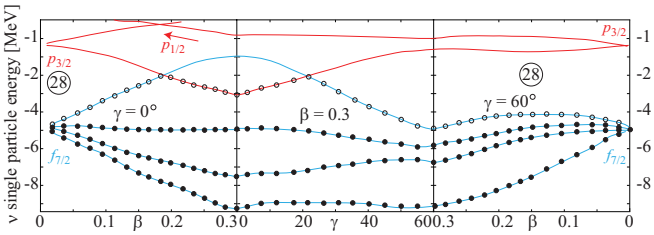

FIG. 3. (Color online) Neutron single-particle energies as a function of the quadrupole deformation parameters β and γ along the fan-shaped path shown in Fig. 2(a). The blue (red) line indicates an orbit originating in the spherical $f_{7/2}$ ($p_{3/2}$) orbit. Lines (with open and solid circles) show unoccupied levels (levels occupied by one and two neutrons).

prolate-deformed $K^\pi = 1/2^-$ ground band, the identification of the $1/2^-_1$ state predicted at 80 keV is essential.

The isomeric $7/2^-_1$ state has different characteristics and mainly consists of $K^\pi = \pm 7/2^-$ states. Figure 2 (d) shows the energy surface of the $K^\pi = 7/2^-$ state and its GCM overlap with the $7/2^-_1$ states. Both the energy surface and the GCM overlap show triaxial deformation of this state, indicating that both normal $(\nu f_{7/2})^{-1}$ and intruder $(\nu p_{1/2})^1$ configurations contribute to it because of the enhanced quadrupole correlation triggered by the quenching of the $N = 28$ shell gap. This result explains the hindered $B(E2)$ between this isomeric state and the ground state, because the K quantum numbers in these states differ by more than 2 ($K^\pi = \pm 1/2^-$ states dominate the ground band, while $K^\pi = \pm 7/2^-$ states dominate the $7/2^-_1$ state), and their deformations also differ. The $9/2^-_1$ and $11/2^-_2$ states have the same characteristics as the $7/2^-_1$ state [see Fig. 2(e) for the $9/2^-$ state]. They are also dominated by the $K^\pi = \pm 7/2^-$ states and the GCM overlaps are concentrated in the triaxially deformed region. An interesting and important point is that the $B(E2)$ between the $7/2^-_1$, $9/2^-_1$, and $11/2^-_2$ states are large enough such that the $7/2^-_1$ state cannot be interpreted as spherical, which is also discussed in Ref. [26]. We also note that the $B(M1)$ values connecting the triaxially deformed states (Table II) are larger than those of the ground band and the shell model prediction [12]. Different from the ground band, the proton orbital angular momentum part contributes to the $M1$ matrix element and it has the same sign as the neutron spin part. Those enhanced $B(E2)$ and $B(M1)$ are further evidence for the deviation of the $7/2^-_1$ state from a spherical shape and its triaxial deformation.

Finally, the energy surface and GCM overlap of the $3/2^-_2$ state are shown in Fig. 2(f). This state exhibits oblate deformation with $\beta < 0.3$ and $\gamma \approx 60^\circ$ and is dominated by the $K^\pi = \pm 3/2^-$ state. The $5/2^-_2$ and $7/2^-_3$ states are also dominated by the $K^\pi = \pm 3/2^-$ state and are classified as oblate states. In these oblate-deformed states, the normal $(\nu f_{7/2})^{-1}$ configuration dominates and the $N = 28$ shell gap remains large. However, the fact that $B(E2)$ is large and the quadrupole moment is not small again indicates deviation from the spherical shape, which will also be important information for experimentally identifying shape coexistence. Similar to the triaxially deformed states, $B(M1)$ values connecting the oblate-deformed states are also enhanced, which is again due to the contribution from the proton orbital angular momentum part. Thus, the coexistence of the prolate-deformed, triaxially deformed, and oblate-deformed states below 2 MeV is predicted. The importance of triaxial deformation of the $7/2^-_1$ state is also confirmed by the axial GCM [Fig. 1(d)]. Although the properties of the prolate-deformed band are qualitatively the same as those obtained by the triaxial GCM, the axial GCM fails to reproduce the excitation energy and the quadrupole moment of the $7/2^-_1$ state ($E_x = 2.1$ MeV and $Q = 6.7\ e^2\ \mathrm{fm}^2$).

To summarize, we investigated the low-lying spectrum of ^{43}S by AMD. The coexistence of prolate-deformed, triaxially deformed, and oblate-deformed states owing to the strong quadrupole correlations triggered by quenching of the $N = 28$ shell gap is predicted. The ground band is a prolate-deformed rotational band with a broken $N = 28$ magicity. On the other hand, the isomeric $7/2^-_1$ state at 319 MeV is interpreted as a triaxial state with a mixture of normal and intruder configurations. An oblate band with a normal configuration starting at the $3/2^-_2$ state at 1.8 MeV is predicted. The calculated prolate-deformed ground state and triaxially deformed $7/2^-_1$ state plausibly explain the available data. Experimental information on the $1/2^-_1$ state, $B(E2; 9/2^-_1 \to 7/2^-_1)$, and the identification of the oblate band will be important for establishing the coexistence of the various deformed states driven by the quenching of the $N = 28$ shell gap.

[1] H. Simon *et al.*, Phys. Rev. Lett. **83**, 496 (1999).
[2] C. Thibault *et al.*, Phys. Rev. C **12**, 644 (1975).
[3] O. Solin and G.-G. Porquet, Prog. Part. Nucl. Phys. **61**, 602 (2008).
[4] O. Sorlin *et al.*, Phys. Rev. C **47**, 2941 (1993).
[5] H. Scheit *et al.*, Phys. Rev. Lett. **77**, 3967 (1996).
[6] T. Glasmacher *et al.*, Phys. Lett. B **395**, 163 (1997).
[7] R. W. Ibbotson, T. Glasmacher, P. F. Mantica, and H. Scheit, Phys. Rev. C **59**, 642 (1999).
[8] F. Sarazin *et al.*, Phys. Rev. Lett. **84**, 5062 (2000).
[9] D. Sohler *et al.*, Phys. Rev. C **66**, 054302 (2002).
[10] B. Bastin *et al.*, Phys. Rev. Lett. **99**, 022503 (2007).
[11] L. Gaudefroy *et al.*, Phys. Rev. C **78**, 034307 (2008).
[12] L. Gaudefroy *et al.*, Phys. Rev. Lett. **102**, 092501 (2009).
[13] L. A. Riley *et al.*, Phys. Rev. C **80**, 037305 (2009).
[14] J. Retamosa, E. Caurier, F. Nowacki, and A. Poves, Phys. Rev. C **55**, 1266 (1997).
[15] D. J. Dean *et al.*, Phys. Rev. C **59**, 2474 (1999).
[16] G. A. Lalazissis, D. Vretenar, P. Ring, M. Stoitsov, and L. Robledo, Phys. Rev. C **60**, 014310 (1999).
[17] S. Péru, M. Girod, and J. F. Ferger, Eur. Phys. J. A **9**, 35 (2000).
[18] R. Rodríguez-Guzmán, J. L. Egido, and L. M. Robledo, Phys. Rev. C **65**, 024304 (2002).
[19] E. Caurier *et al.*, Rev. Mod. Phys. **77**, 427 (2005).
[20] L. Gaudefroy, Phys. Rev. C **81**, 064329 (2010).
[21] K. Kaneko, Y. Sun, T. Mizusaki, and M. Hasegawa, Phys. Rev. C **83**, 014320 (2011).
[22] Z. P. Li *et al.*, Phys. Rev. C **84**, 054304 (2011).
[23] T. R. Rodríguez and J. L. Egido, Phys. Rev. C **84**, 051307(R) (2011).

[24] K. Heyde and J. L. Wood, Rev. Mod. Phys. **83**, 1467 (2011).
[25] D. Santiago-Gonzalez I. Wiedenhöver, V. Abramkina, M. L. Avila, T. Baugher, D. Bazin, B. A. Brown, P. D. Cottle, A. Gade, T. Glasmacher, K. W. Kemper, S. McDaniel, A. Rojas, A. Ratkiewicz, R. Meharchand, E. C. Simpson, J. A. Tostevin, A. Volya, and D. Weisshaar, Phys. Rev. C **83**, 061305 (2011).
[26] R. Chevrier *et al.*, Phys. Rev. Lett. **108**, 162501 (2012).
[27] Y. Kanada-En'yo and H. Horiuchi, Phys. Rev. C **66**, 024305 (2002).
[28] Y. Kanada-En'yo, M. Kimura, and H. Horiuchi, C. R. Phys. **4**, 497 (2003).
[29] Y. Kanada-En'yo, Phys. Rev. C **85**, 044320 (2012).
[30] M. Kimura and H. Horiuchi, Prog. Theor. Phys. **111**, 841 (2004).
[31] M. Kimura, Phys. Rev. C **75**, 041302 (2007).
[32] K. Minomo *et al.*, Phys. Rev. Lett. **108**, 052503 (2012).
[33] J. Dechargé and D. Gogny, Phys. Rev. C **21**, 1568 (1980); J. F. Berger, M. Girod, and D. Gogny, Comp. Phys. Commun. **63**, 365 (1991).
[34] M. Kimura, Phys. Rev. C **69**, 044319 (2004).
[35] T. Suhara and Y. Kanada-En'yo, Phys. Rev. C **82**, 044301 (2010).
[36] M. Kimura *et al.*, Prog. Theor. Phys. **127**, 287 (2012).
[37] G. Neyens, Phys. Rev. C **84**, 064310 (2011), and references therein.
[38] Andreyev *et al.*, Nature (London) **405**, 430 (2000).
[39] A. Dóte, H. Horiuchi, and Y. Kanada-En'yo, Phys. Rev. C **56**, 1844 (1997).